npj | 2D materials and applications

www.nature.com/npj2dmaterials

ARTICLE OPEN

# Fundamentals of low-resistive 2D-semiconductor metal contacts: an ab-initio NEGF study

Rutger Duflou[1,2,3], Geoffrey Pourtois[1], Michel Houssa[1,2] and Aryan Afzalian[1,3]✉

Metal contacts form one of the main limitations for the introduction of 2D materials in next-generation scaled devices. Through ab-initio simulation techniques, we shed light on the fundamental physics and screen several 2D and 3D top and side contact metals. Our findings highlight that a low semiconducting-metal contact resistance can be achieved. By selecting an appropriate 2D metal, we demonstrate both ohmic or small Schottky barrier top and side contacts. This leads to a contact resistance below 100 Ωμm and good device drive performance with currents in ON state up to 1400 μA/μm, i.e., reduced by a mere 25% compared to a reference with perfect ohmic contacts, provided a sufficiently high doping concentration of $1.8\times10^{13}\,cm^{-2}$ is used. Additionally, we show that this doping concentration can be achieved through electrostatic doping with a gate. Finally, we perform a screening of possible 2D–3D top contacts. Finding an ohmic 2D–3D contact without a Schottky barrier has proven difficult, but it is shown that for the case of intermediate interaction strength and a limited Schottky barrier, contact resistances below 100 Ωμm can be achieved.

*npj 2D Materials and Applications* (2023)7:38 ; https://doi.org/10.1038/s41699-023-00402-3

## INTRODUCTION

Transistors made of novel two-dimensional (2D) semiconducting materials[1], i.e., an atomically thin layer of material that does not create strong atomic bonds in the third dimension, such as transition-metal dichalcogenides (TMD)[2–5], are being actively investigated as future replacement of Si as channel materials. Finding a metal with a low Schottky barrier to achieve a low contact resistance is one of the key challenges to address towards 2D material CMOS. Two main schemes of contacting are possible: top and side contacts (TC and SC, respectively).

TC are typically used in Si CMOS technologies as they enable a larger contact area, hence a lower resistivity. Due to their specific nature, this poses a special challenge for 2D material channel materials. The proximity of a 3D metal with strong affinity and binding energy may affect the chemical nature of the underlying 2D material. This typically results in an important density of interfacial traps (DIT) that pins the Fermi level ($E_F$) at the semiconductor-metal interface. As a result, a high Schottky barrier height ($SB_H$), hence a high contact resistance is achieved. Using a low-binding-energy metal, such as a 2D metal, on the other hand, 2D metal/2D semiconductor van der Waals (vdW) contacts have been shown to be an interesting option, as they may be free of Fermi-level pinning[6]. In such a contact, the expected $SB_H$ should be in accordance with the Schottky–Mott theory, dictated by parameters like the metal work function and the semiconductor electron affinity, and low $SB_H$ could be achieved by a proper material selection. Due to limited out-of-plane bonding, injection of carriers into the device with metals deposited on top of the 2D material may be limited by vdW tunneling. SC are not limited by a vdW gap for carrier injection. However, fabrication of SC has proven to be more challenging leading to higher device variation[6]. Additionally, covalent bonding can again give rise to higher $SB_H$, even in the case of 2D–2D interfaces. Using ab initio techniques, based on advanced Density Functional Theory (DFT) and Non-equilibrium Green's function (NEGF) transport simulations, we perform, here, using our atomistic solver ATOMOS[7,8], a thorough dissipative DFT-NEGF theoretical study of 2D metal–2D semiconductor contacted transistors to explore and understand their physics and fundamental performance limit. Additionally, we perform an initial screening of 3D metal–2D semiconductor interfaces, focusing on interfaces demonstrating intermediate behavior, i.e., an interaction strength high enough to limit the influence of the vdW gap, but low enough to limit the Fermi-level pinning.

## RESULTS

### Material and device choices

In this study, we focus on two options for the semiconducting TMD: $WS_2$ (in its most stable 2H phase) and $HfS_2$ (in its most stable 1T phase). $WS_2$ is one of the most studied 2D materials and shows great promise with reasonably high theoretical predictions for both its n-type and p-type mobility[8]. $HfS_2$ is a relatively less known material, with fewer experimental results, but is predicted to have an exceptionally high mobility and a higher drive current, while maintaining good scalability down to 5 nm gate lengths[8]. We investigate several device configurations depending on the type of metal–semiconductor contacts. For 2D–2D TC and SC, we consider a single independent contact as well as a full transistor configuration. The single contact allows for an estimate of the contact resistance by dividing the applied bias by the current through the contact. For the full transistor, both a dual-gate (DG) MOSFET and a dynamically doped field-effect transistor ($D_2$-FET) device, i.e., an individually back-gated transistor that does not require a spacer and allows for dynamically doping the source and drain extension with its gate (Fig. 1b, d)[8], are simulated. For 2D–3D contacts, we are limited to a single contact configuration as the significant computational cost prohibits a full transistor simulation. All device structures simulated in ATOMOS are shown in Fig. 1. In all transistor simulations, the gate length is $L = 14$ nm. The gate oxide has a relative permittivity $\varepsilon_R = 15.6$, corresponding to a lower bound estimate for $HfO_2$, and thickness of 2 nm, resulting in

[1]imec, Kapeldreef 75, 3001 Leuven, Belgium. [2]Department of Physics and Astronomy, KU Leuven, Celestijnenlaan 200D, 3001 Leuven, Belgium. [3]These authors contributed equally: Rutger Duflou, Aryan Afzalian. ✉email: Aryan.Afzalian@imec.be

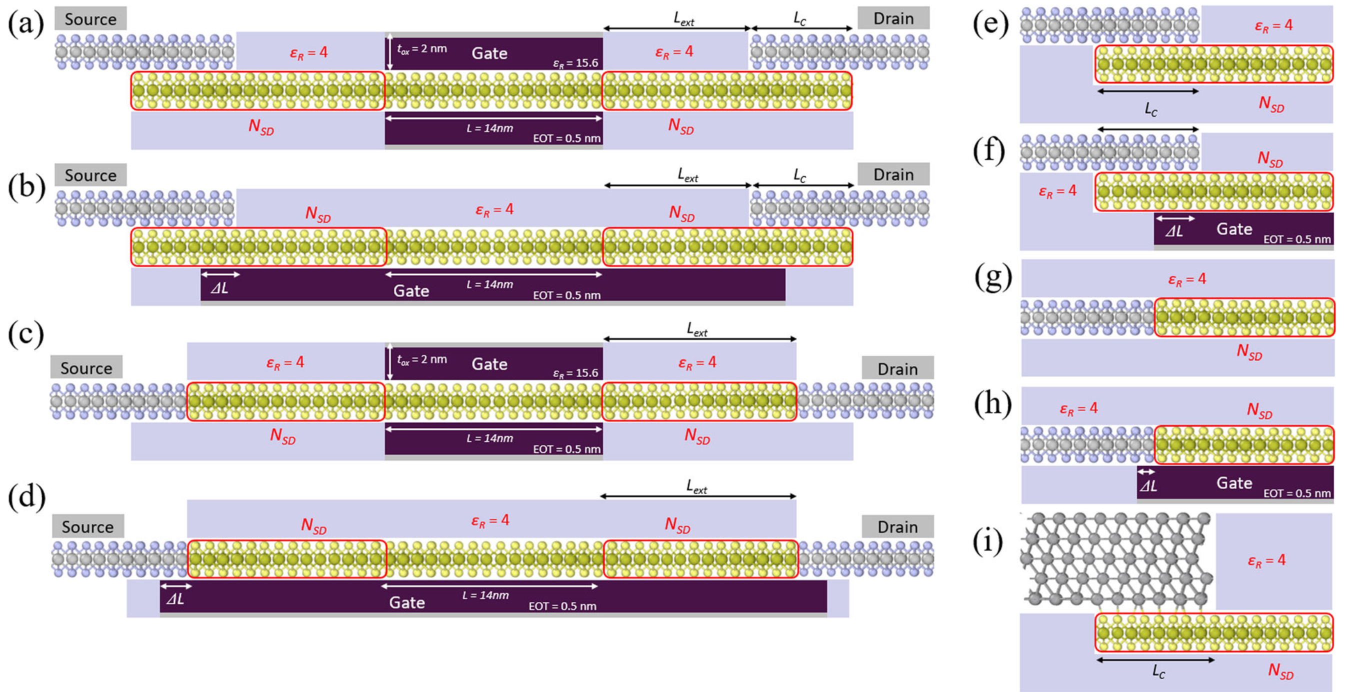


**Fig. 1 Schematic views of the different devices simulated in ATOMOS. a**, **b** represent, respectively, the DG-MOSFET and $D_2$-FET with a single TMD layer for the channel and 2D–2D TC at the source and drain. **c**, **d** represent, respectively, the DG-MOSFET and $D_2$-FET with 2D–2D SC. **e**, **f** (**g**, **h**) represent a single 2D–2D TC (SC) with, respectively, chemical and dynamic doping, while **i** represents a single 2D–3D TC.

an equivalent oxide thickness EOT = 0.5 nm. The source-drain bias is set at $V_D = 0.6$ V, unless specified otherwise. For single contact simulations, the source and drain are ill-defined and $V_D$ and $V_{GS}$ denote respectively the bias applied over the contact and the potential difference between the doping gate, if present, and the metallic part of the system. The metal contacts and source- and drain- (S&D) extensions are surrounded by a low-K spacer oxide with $\varepsilon_R = 4$. In all cases, only the source-drain metal contacts and the 2D channel material were explicitly included in the atomistic simulation domain (part with atoms as shown in Fig. 1). Simulating the metal in the gate stack and micron-long metal interconnects connecting to the source and drain is outside the scope of this work. This implies that we forgo the effect of the metal resistance in the interconnects, the gate leakage current through the gate oxide and a direct calculation of the threshold voltage as determined by the gate metal work function. For the interconnect resistance, considering that some of the low Schottky-barrier contact metals used here are not conventionally used as interconnects, we have verified that extending the lengths of these metallic regions to several tens of nanometers, which would be sufficient to switch to another more conventional interconnect metal, does not degrade the contact resistances (see Supplementary Note 1 for more details). The gate oxide was not simulated atomistically but included as a continuum region with a thickness and a permittivity value in our Poisson solver. The discussion on the gate leakage current could be alleviated by noting that a lower bound estimate for the permittivity of $HfO_2$ was used. Using an upper bound estimate of 25 for $HfO_2$, allows us to increase the oxide thickness to 3.2 nm for the same EOT, significantly reducing gate leakage, with virtually no changes to the results we present here. The work function of the metal gate is typically adjusted to shift the threshold voltage and achieve a fixed $I_{OFF}$ value at a gate voltage bias $V_{GS} = 0$ V. The relative shift compared to a purely semiconducting TMD simulation with perfect ohmic contacts is reported in the Supplementary Table 2. Finally, in this work, electron-phonon scattering was included in all the simulations, using the self-consistent Born approximation[8], as detailed in the "Methods" section.

## 2D–2D top-contact configuration

For $HfS_2$, $HfTe_2$ (1 T) was found to be an interesting n-type contact candidate with a low Schottky barrier. The results for a single contact and for the DG device with chemical doping are summarized in Fig. 2. Figure 2a demonstrates the influence of the doping concentration on the contact resistance in a single TC configuration. The contact resistances for doping concentrations of $1.8\times10^{13}\,cm^{-2}$ and $3\times10^{13}\,cm^{-2}$ are respectively 90 Ωμm and 50 Ωμm and are largely independent of the bias. These values are comparable with the quantum limit of 20–30 Ωμm at these doping concentrations[9]. When the doping concentration is reduced, the value of the contact resistance rapidly increases. An average value of 370 Ωμm is observed at $6\times10^{12}\,cm^{-2}$ and $R_C \sim 10$ kΩμm at $6\times10^{11}\,cm^{-2}$. Also the dependency of the contact resistance on the bias increases significantly. Figure 2b shows the influence of the contact overlap length, $L_C$. The contact resistance shows a rapid decrease with increasing values of $L_C$ for very low values of $L_C$. The contact resistance then saturates to a constant value when $L_C$ is increased further, due to current crowding[10]. Extracting an accurate estimate of the transfer length, i.e., the length for which this transition from decreasing to constant $R_C$ happens, is made non-trivial by the presence of oscillations of $R_C$ when sweeping $L_C$. These oscillations are attributed to coherent interference effects related to the wave nature of electrons, described in more detail in Supplementary Note 4. It is, however, evident that the dependency of the contact resistance on $L_C$ is small as long as $L_C$ is larger than a few nanometers. This implies that injection can be considered as edge injection despite the low Schottky barrier height. Figure 2c shows the current for a DG-MOSFET in comparison with a device with perfect ohmic contacts and a device with highly-doped $HfS_2$ second layer regions acting as metallic TC. We find that the introduction of $HfTe_2$ TC reduces the current by about 60% compared to the device with perfect ohmic contacts. From the density of states (DOS) of the device in

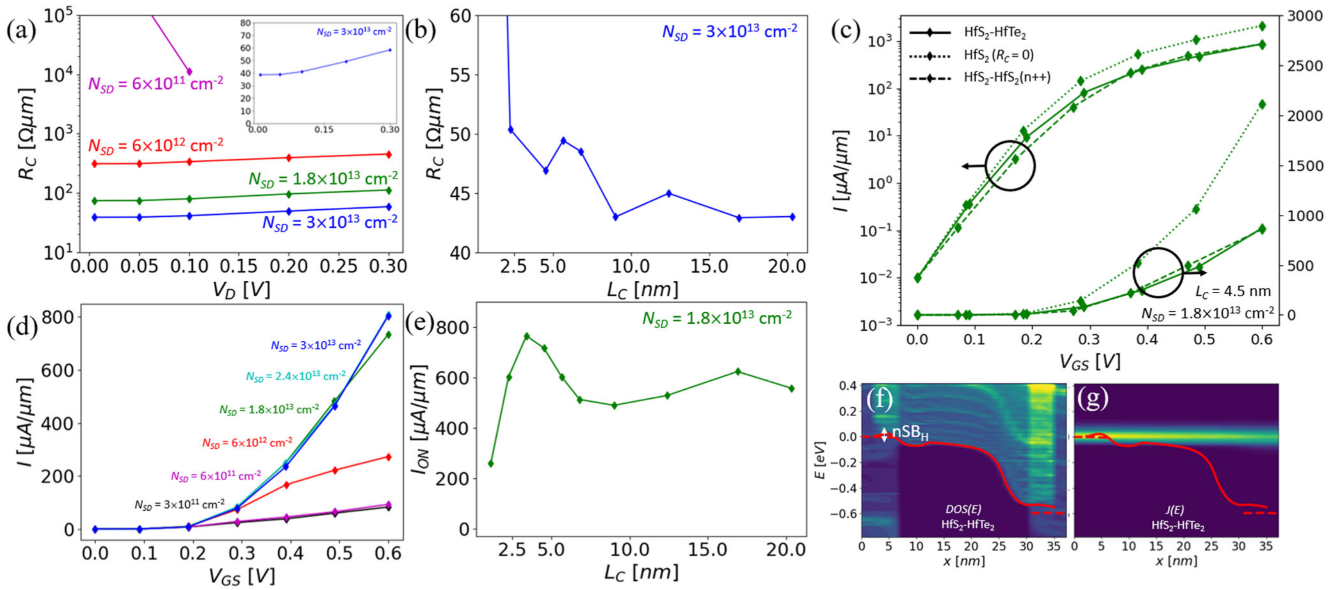

**Fig. 2 Results for the $HfS_2$-$HfTe_2$ TC.** **a** shows the contact resistance as a function of the bias for several doping concentrations for $L_C = 4.5$ nm, the inset showing the results for the highest doping on a linear scale. **b** shows the influence of $L_C$ on $R_C$ for $N_{SD} = 3\times10^{13}\,cm^{-2}$. **c** shows the IV curve for a DG-MOSFET with $L_C = 4.5$ nm, $L_{ext} = 4.9$ nm and $N_{SD} = 1.8\times10^{13}\,cm^{-2}$ as well as the IV for a reference case with ohmic contacts and a reference case using a highly doped $HfS_2$ layer for the metal TC ($N_{SD} = 4.2\times10^{13}\,cm^{-2}$ in the top layer. We observed a saturation of the contact resistance when $N_{SD}$ was increased above $3\times10^{13}\,cm^{-2}$ for either the top or bottom layer). **d**, **e** show, respectively, the current and $I_{ON}$, at a fixed $I_{OFF}$ and $V_D$ of 0.01 μA/μm and 0.6 V, respectively, for several values of $N_{SD}$ and $L_C$ to demonstrate the influence of doping concentration and contact overlap length. The current is normalized by the gate perimeter, i.e., the current is divided by the gate width times the number of gates, as typically reported in the literature. **f**, **g** show, respectively, the DOS and current spectrum within the device. The full red line denotes the bottom of the conduction band in the semiconductor and the dashed lines denote the Fermi level in the metal.

equilibrium without doping, we can extract an estimate of the Schottky barrier height of $nSB_H = 40$ meV. This $SB_H$ is further reduced at the source side under operating conditions, owing to the Fermi-level degeneracy in the conduction band induced by the high doping concentration, as can be seen in Fig. 2f, g. A more in-depth discussion of the Schottky barrier lowering can be found in Supplementary Note 5. Considering the lowered Schottky barrier, the reduction in current can mostly be attributed to the vdW gap. This is confirmed by the results on the $HfS_2$ DG-nMOSFET with highly-doped $HfS_2$ TC, that mimic ohmic vdW contacts. This reference case does not have a Schottky barrier but demonstrates a similar current reduction. Figure 2d, e demonstrate the influence of doping concentration and the length of the TC overlap region. A doping concentration of $1.8\times10^{13}\,cm^{-2}$ is required to preserve the ON-current ($I_{ON}$). Increasing the doping concentration beyond this value increases $I_{ON}$, but the benefits appear less significant than for the single contact and the effect saturates at $N_{SD} = 3\times10^{13}\,cm^{-2}$. $I_{ON}$ shows a peak around $L_C = 4.5$ nm, but little dependency on $L_C$ for higher values of $L_C$, affirming that injection happens through edge injection. We thus find that the conditions under which the transport simulations were performed were close to ideal. Consequently, doping concentration and contact overlap length do not provide a means to significantly alleviate the 60% reduction in $I_{ON}$ imposed by the vdW contact. All values extracted from these and the following simulations are summarized in Supplementary Tables 1 and 2.

For $WS_2$, finding an adequate n-type TC has proven challenging. Three metallic TMDs were selected as possible TC candidates: $WTe_2$ (1T′), $MoTe_2$ (1T′) and $NbS_2$ (2H). The results for a single contact are shown in Fig. 3a, b. $L_C$ was set to 4.5 nm based on our findings on the $HfS_2$-$HfTe_2$ TC. The contact resistances for n-type doped $WS_2$ are all extremely high, even for the high doping concentration of $N_{SD} = 3\times10^{13}\,cm^{-2}$. As a reference, also the contact resistance of a highly-doped $WS_2$ layer as TC is shown, demonstrating that contact resistances as low as 45 Ωμm could be achieved for n-type $WS_2$ by finding a vdW metal with the correct work function. For p-type contacts, $NbS_2$ is found to be an interesting candidate, showing contact resistances of 150 Ωμm and 100 Ωμm for doping concentrations of respectively $1.8\times10^{13}\,cm^{-2}$ and $3\times10^{13}\,cm^{-2}$. Similarly to $HfS_2$-$HfTe_2$, the contact resistance increases rapidly when the doping concentration is reduced, showing average contact resistances of 370 Ωμm at $N_{SD} = 6\times10^{12}\,cm^{-2}$ and ~5k Ωμm at $N_{SD} = 6\times10^{11}\,cm^{-2}$.

Figure 3c–j show the results for the DG-MOSFET. The device parameters were chosen based on our findings on $HfS_2$-$HfTe_2$ TC. $N_{SD}$ was set to $1.8\times10^{13}\,cm^{-2}$, $L_{ext}$ to 4.2 nm and $L_C$ to 4.5 nm. The DOS in the simulation was used to extract an estimate of the $SB_H$. The $SB_H$ for $WS_2$-$WTe_2$ and $WS_2$-$MoTe_2$ are found to be around 500 meV under operating conditions, as can be seen in Fig. 3e, f. The large contact resistances are attributed to the presence of a significant Schottky barrier height on top of the tunneling barrier imposed by the vdW gap. These lead to severe $I_{ON}$ reductions by respectively a factor 1000 and 10,000, when compared to the reference case with perfect ohmic contacts of Fig. 3c. To provide an additional reference, we discuss a TC configuration with highly doped $WS_2$ for the metal, which is also characterized by a vdW gap but does not have a Schottky barrier. As a result, $I_{ON}$ is only reduced by 25%, complying with the low contact resistance found for these TC.

$WS_2$-$NbS_2$ is characterized by a negative value for $pSB_H$ and, hence, provides an ohmic p-type TC. Despite this ohmic contact, $I_{ON}$ is reduced by 95% under normal operating conditions of $|V_D| = 0.6$ V. When $|V_D|$ is lowered to 0.15 V, the reduction is found to be only 50%. An explanation of this phenomenon can be found in the DOS and current spectrum of the device. $NbS_2$ is a cold metal with no high energy carriers, which is denoted by the gap in the DOS of the left-most and right-most parts of Fig. 3g, i. At low

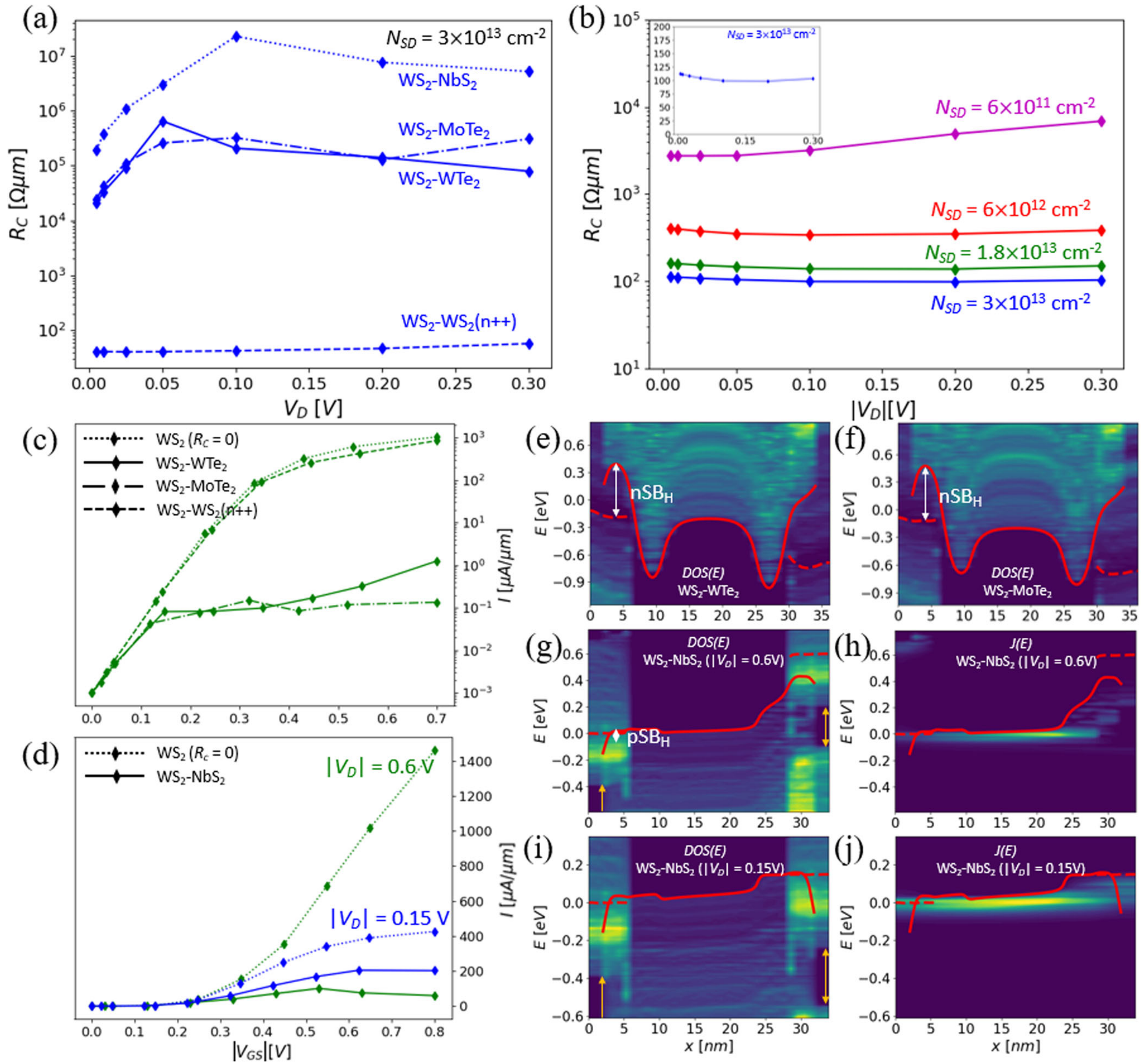


**Fig. 3 Results for the WS2 2D–2D TC.** The metals for the TC are either $WTe_2$, $MoTe_2$ or $NbS_2$. $L_C = 4.5$ nm and for the DG-MOSFET $L_{ext} = 4.2$ nm and $N_{SD} = 1.8\times10^{13}\,cm^{-2}$. **a** shows the contact resistances for n-type doped $WS_2$ with $N_{SD} = 3\times10^{13}\,cm^{-2}$, in combination with $MoTe_2$, $WTe_2$ and $NbS_2$ as well as a highly doped $WS_2$ layer as a reference. **b** shows the contact resistances for p-type doped $WS_2$ in combination with $NbS_2$ for various doping concentrations, the inset showing the results for the highest doping on a linear scale. **c** shows the IV curves for the n-type DG-MOSFETS as well as for a reference case with ohmic contacts and a reference case with highly doped $WS_2$ for the metal TC. **d** shows the IV curves for the p-type DG-MOSFETS with similar references with ohmic contacts. **e**, **f** show the DOS of the DG-MOSFET with, respectively, $WTe_2$ and $MoTe_2$ TC. The full red line denotes the bottom of the conduction band in the semiconductor and the dashed lines denote the Fermi level in the metal. **g**, **h** show, respectively, the DOS and current spectrum within the device with $NbS_2$ TC under normal bias conditions, while **i**, **j** show the DOS and current spectrum when the source-drain bias is lowered. In these graphs, the full red lines denote the top of the valence band and the orange arrows denote the DOS gap.

bias, this has little influence on the current. However, at high bias, the energy at which carriers are injected at the source is similar to the energy of the drain-side gap. Therefore, carriers cannot be ballistically extracted at the drain side and the current is reduced. A more in-depth discussion is provided in ref. [11]. It should be noted that such behavior emerges only in full device simulations when both contacts are made of the same cold metal and not in the simulation of a single contact, or if a more complex device scheme with asymmetric source and drain contacts would be used[11]. This shows the importance of full device simulations, where possible, as the extraction of contact resistances alone can neglect physics important for device performance. It is interesting to note that the contact resistances for the $WS_2$-$NbS_2$ TC are larger than the ones found for the $HfS_2$-$HfTe_2$ TC. However, the reduction of $I_{ON}$ is slightly less severe for the $WS_2$ device with $NbS_2$ TC than for the $HfS_2$ device with $HfTe_2$ TC. This may be attributed to the better transport property of $HfS_2$. This results in a lower channel resistance in series with $R_C$, and hence a greater influence of $R_C$ despite its lower value. A second thing to note is that $HfS_2$ with $HfTe_2$ TC showed a similar reduction in $I_{ON}$ as the $HfS_2$ reference


Published in partnership with FCT NOVA with the support of E-MRS

case with highly doped $HfS_2$ TC, implying that the contact resistance is mostly the results of the vdW gap. The $WS_2$-$WS_2$(n ++) TC and $WS_2$-$NbS_2$ TC are also characterized by similar vdW gaps. Indeed, the interlayer coupling is found to be almost identical. Despite this, $WS_2$-$NbS_2$ shows a much greater reduction of $I_{ON}$ than $WS_2$-$WS_2$(n ++). A possible explanation can be found in the necessity of k-matching. This means that ballistic transmission through the contact or even the full device, does not only require states at the same energy at injection and extraction, but also requires states at the same k-point. This requirement is not exclusive to cold-metal based devices but can be more relevant for such transistors as the band structure of cold metals often consists of one band at the Fermi level. Hence, at a specific energy, states are only available at certain k-points. Additionally, in contrast to the cold-metal behavior discussed above which only arises in full devices, the requirement for k-matching is also relevant for single contacts. This explains the larger contact resistance for the $WS_2$-$NbS_2$ TC than for the $WS_2$-$WS_2$(n ++) or $HfS_2$-$HfTe_2$ TC. A more in-depth discussion is provided in Supplementary Note 6.

It should be noted that Fig. 3g–j show potential peaks at the edge of the semiconducting material. These peaks are the result of charge build-up due to unpassivated dangling bonds related to the abrupt termination of the 2D semiconducting material, at the 1st and last layers in the transport direction ($x$), in our simulations. The charge corresponding to these dangling bonds effectively gives rise to a potential peak, which, in the case of some material systems, like for $WS_2$-$NbS_2$ in Fig. 3, gives rise to an additional barrier for carriers. This extra barrier is only of importance when the overlap length is very small, such that it overlaps with the region of injection. However, due to transfer lengths being small and that we, hence, mostly have edge injection, an overlap region of several nanometers, such as those used in this work, is found to be sufficient for our IV results to be independent of the type of passivation (or non-passivation) used for the edges. A more elaborate discussion is also provided in Supplementary Note 7.

## 2D–2D side-contact configuration

For the 2D–2D SC configuration, we limit ourselves to $HfS_2$-$HfTe_2$ and $WS_2$-$NbS_2$ as these provided low Schottky-barrier heights for the ideal case of vdW contacts. The results for the single contact simulations are shown in Fig. 4a, b. For both material combinations, the results strongly depend on the doping concentration. $HfS_2$-$HfTe_2$ SC show significantly lower contact resistances than the $WS_2$-$NbS_2$ SC. For doping concentrations of respectively $1.8\times10^{13}\,cm^{-2}$ and $3\times10^{13}\,cm^{-2}$, the contact resistance of the $HfS_2$-$HfTe_2$ SC is largely independent of the bias and has values of respectively 75 Ωμm and 38 Ωμm. For a doping concentration of $6\times10^{12}\,cm^{-2}$, both the average value of the contact resistance and its susceptibility to the bias increase significantly, with an average value of around 500 Ωμm. Note that for low doping concentrations, the SC has a higher contact resistance than the TC, while for a high doping concentration the SC has a lower contact resistance. For $WS_2$-$NbS_2$ SC, the average value as well as the susceptibility to the bias is large, even in the case of high doping concentrations.

Figure 4c–h shows the results for the $HfS_2$ and $WS_2$ DG-MOSFET with, respectively, $HfTe_2$ and $NbS_2$ SC. The S&D extensions have length $L_{ext} = 9$ nm and are doped with a doping concentration of $N_{SD} = 1.8\times10^{13}\,cm^{-2}$. $V_D$ is limited to 0.15 V for the $WS_2$ device to suppress any reduction effect related to the cold metallic nature of $NbS_2$. Figure 4e, g denote the DOS for both systems. The $SB_H$'s are both around 100 meV. The formation of covalent bonds at the $HfS_2$-$HfTe_2$ or $WS_2$-$NbS_2$ interface gives rise to moderate Fermi level pinning, mildly increasing the $SB_H$ compared to the ideal vdW contact. In that regard, the 2D metals used here may have an advantage over other SC metals as they provide a very clean atomic interface, sharing either a same Hf or S atom for the $HfS_2$-$HfTe_2$ or $WS_2$-$NbS_2$ cases respectively. Despite the similar $SB_H$, the current spectra, denoted in Fig. 4f, h, demonstrate significantly different behavior. For the $HfS_2$-$HfTe_2$ system, the current passes through the Schottky barrier quasi ballistically, while for the $WS_2$-$NbS_2$, the current is strongly scattered. The IV curves are shown in respectively Fig. 4c, d. For $HfS_2$-$HfTe_2$, the SC perform better than the TC, showing a reduction of $I_{ON}$ of only 25% instead of 60% for the TC. For $WS_2$-$NbS_2$ the SC perform significantly worse than the TC, showing a reduction of $I_{ON}$ of 85% instead of 50%. This complies with the contact resistances in Fig. 4a, b. The more severe $I_{ON}$ reduction and the strong presence of scattering for $WS_2$-$NbS_2$ can be linked to the need for k-matching, discussed in further detail in Supplementary Note 6.

## Dynamic doping

The discussion on TC showed that sufficient doping concentration is required to allow for tunneling through the vdW gap. A high doping concentration is known to increase the number of available carriers and the electric field, and hence to promote tunneling[12]. For SC, there is no vdW gap, but there is a significant $SB_H$. Sufficient doping is required to thin the Schottky barrier. Figure 1 showed how a gate can be used to achieve dynamic doping[8,13] in $D_2$-FETs and single contacts. For both 2D–2D TC and 2D–2D SC, $HfS_2$-$HfTe_2$ contacts provided the lowest contact resistance and demonstrated good device performance. Figure 5 demonstrates how the contact resistances are influenced when a doping gate is used. The chemical doping concentration is set to the intrinsic doping concentration $N_{SD} = 6\times10^{11}\,cm^{-2}$. Figure 5a, c show how the carrier concentration increases, and hence, the contact resistance decreases, as the gate potential is increased. However, for the single contact case, the carrier concentration depends not on $V_{GS}$, but on the difference between the gate potential and the potential in the TMD, i.e., $V_{GS}$-$V_D$. The contact resistance thus depends strongly on the bias even in the case of high carrier concentrations. Additionally, Fig. 5a, c show that carrier concentrations of ~$1.8\times10^{13}\,cm^{-2}$ can be reached. The contact resistances can reach values as low as 50 Ωμm for TC and 55 Ωμm for SC. Note that these values are lower than the respective $R_C$ values obtained for the single contacts with chemical doping concentrations of $1.8\times10^{13}\,cm^{-2}$. In addition to providing the required carrier concentration, the doping gate thus lowers the contact resistance through other methods, presumably through creating additional electric fields which are beneficial for tunneling. The effect appears most pronounced for the TC as the $R_C$ value reached are even lower than the values found for $N_{SD} = 3\times10^{13}\,cm^{-2}$. Supplementary Fig. 6 shows that these carrier concentrations and contact resistances are achieved for a bias of $V_{GS}$-$V_D = 0.9$ V. For a moderate bias of $V_{GS} - V_D = 0.6$ V, we find a carrier concentration of ~$1\times10^{13}\,cm^{-2}$ and contact resistances of 105 Ωμm and 115 Ωμm for, respectively, TC and SC. Figure 5b, d demonstrate the importance of the overlap length of the doping gate, $\Delta L$. For both SC and TC, the contact resistance deteriorates when the doping gate does not fully reach the metal contact, i.e., $\Delta L < 0$. For the TC, it is found that the doping gate best extends beyond the metal, with $R_C$ decreasing up to $\Delta L = 2.5$ nm. For the SC, the importance of $\Delta L$ is less severe, and a small extension below the metal of $\Delta L = 0.5$ nm is found to be sufficient.

Figure 6 demonstrates the effect of adding a doping gate to a complete transistor. The $D_2$-FET is compared to the DG-MOSFET for both $HfS_2$-$HfTe_2$ TC and SC. For both cases, the DG-MOSFET with intrinsic doping, $N_{SD} = 6\times10^{11}\,cm^{-2}$, demonstrates a low $I_{ON}$. The discussion above showed that for both SC and TC, the contact resistance is very large for such low doping concentrations. Additionally, even with perfect contacts, a source extension with such low doping concentration would also suffer from source starvation and reduced $I_{ON}$ values[8]. For both types of contacts, the $D_2$-FET manages to supply the required carrier concentration to

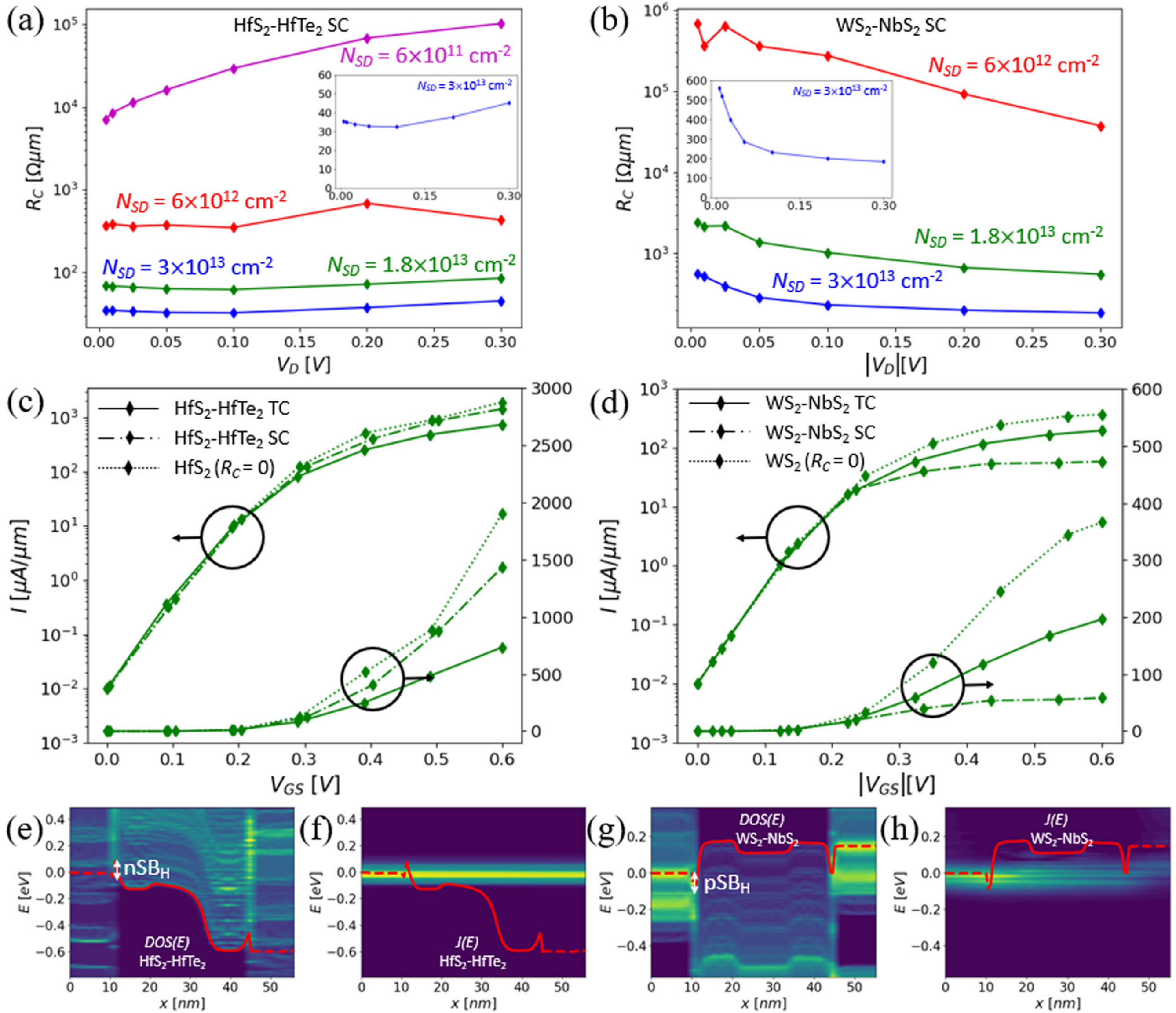


**Fig. 4 Results for the 2D–2D SC.** The contact resistances of the single contacts are shown as a function of the bias for several values of the doping concentration, the insets showing the results on a linear scale. **a** shows the contact resistances for n-type doped $HfS_2$-$HfTe_2$ SC. **b** shows the contact resistances for p-type doped $WS_2$-$NbS_2$ SC. **c** IV curves for the $HfS_2$ DG-MOSFET with $HfTe_2$ SC and TC, as well as the perfect ohmic contact reference case, **d** IV curves for the $WS_2$ DG-MOSFET with respectively $NbS_2$ SC and TC, as well as the perfect ohmic contact reference case. **e**, **f** (**g**, **h**) denote, respectively, the DOS and current spectrum in the $HfS_2$ ($WS_2$) DG-MOSFET.

lower the contact resistance and restore the current in ON state. It is interesting to note that for the TC, the $D_2$-FET also shows significantly better performance than the DG-MOSFET for $N_{SD} = 1.8\times10^{13}\,cm^{-2}$. However, our results in Fig. 2d showed that increasing the doping concentration beyond $N_{SD} = 1.8\times10^{13}\,cm^{-2}$ added little benefit. Hence, any additional carrier concentration increase by the doping gate should not influence the results significantly. Additionally, the $D_2$-FET and DG-MOSFET with SC show very similar results for $N_{SD} = 1.8\times10^{13}\,cm^{-2}$. Finally, the $D_2$-FET with intrinsic doping slightly surpasses the performance of the DG-MOSFET with $N_{SD} = 1.8\times10^{13}\,cm^{-2}$ for the TC. For the SC, however, the $D_2$-FET with intrinsic doping does not reach the $I_{ON}$ of the DG-MOSFET with $N_{SD} = 1.8\times10^{13}\,cm^{-2}$. The explanation for this discrepancy is linked to the additional contact resistance lowering by the doping gate. Our results in Fig. 5 showed that the doping gate lowers the contact resistance through other methods than supplying the required carrier concentration and that this effect is more pronounced for TC. This explains why the $D_2$-FET outperforms the DG-MOSFET for the TC configuration despite a higher doping concentration providing little benefit, and it explains why this is not true for the SC configuration. The reason for the different influence of the doping gate on TC and SC is linked to the different mechanism limiting the current, i.e., vdW tunneling for the top contact which is more sensitive to electric field enhancement and Schottky barrier tunneling for the side-contact which is more sensitive to doping though thinning of the $SB_H$.

For TC, the top metal prevents the introduction of a second doping gate. For SC, a top doping gate can be introduced, by using, for instance, the compact doubled-forked ($E_2$) dynamically doped $E_2D_2$-FET architecture[13]. The device configuration as well as the corresponding contact resistances and device currents are shown in Fig. 7. As expected, the introduction of a second doping gate doubles the carrier concentration to $3.6\times10^{13}\,cm^{-2}$ reduces the contact resistance to a minimum value of 25 Ωμm. Supplementary Fig. 6 shows that this is for a bias of

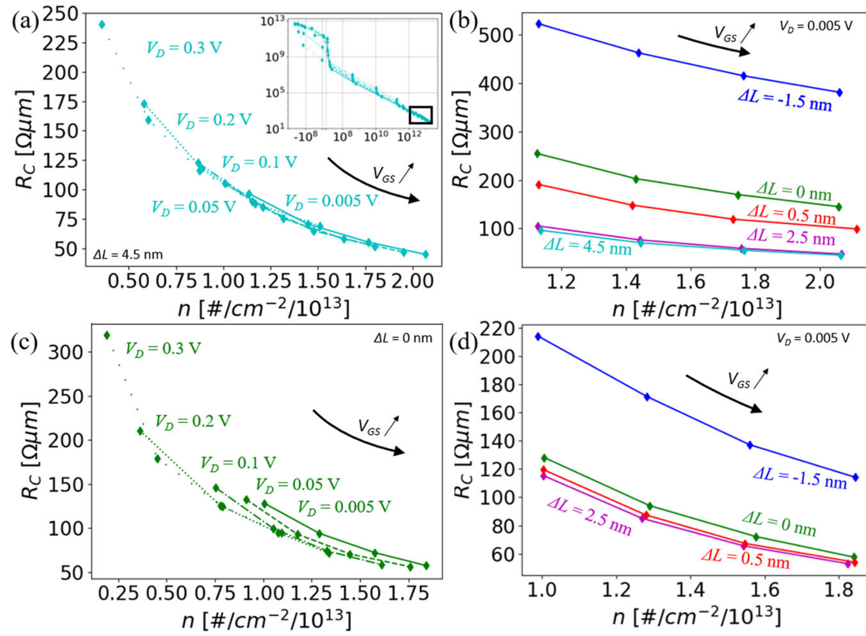


**Fig. 5 Results of dynamic doping simulations for $HfS_2$-$HfTe_2$ contacts.** The contact resistances and carrier concentration for a single $HfS_2$-$HfTe_2$ 2D–2D contact as a function of the doping gate bias are shown. **a**, **b** show the results for TC, **c**, **d** show the results for the SC. **a**, **c** show the results for several values of the bias applied over the resistance. **b**, **d** show the results for several choices of the doping gate overlap length $\Delta L$. The inset in **a** shows the results on a logarithmic scale.

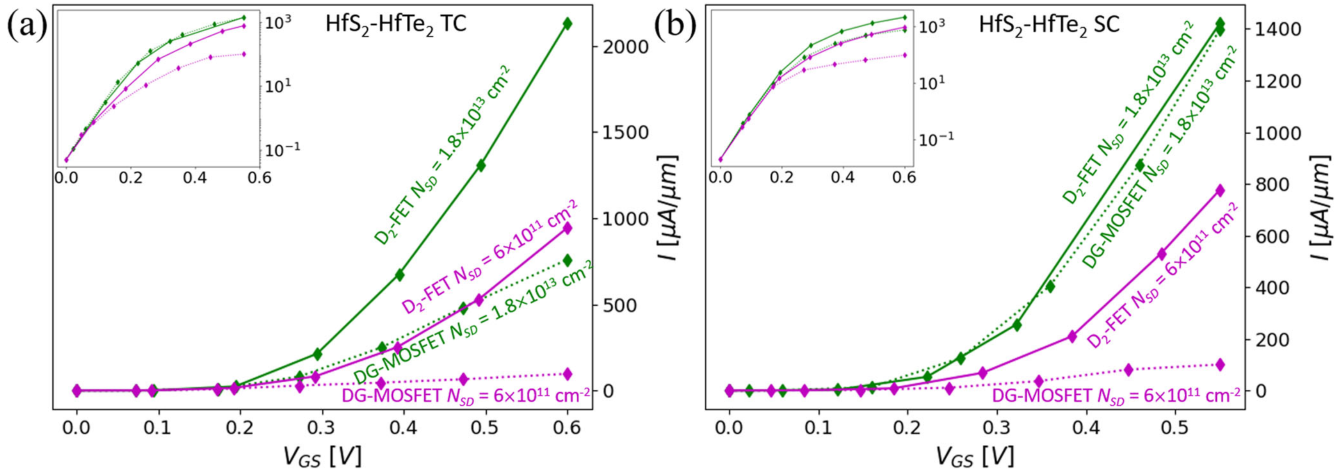


**Fig. 6 Comparison between chemically and dynamically doped transistors.** IV curves for a $HfS_2$ DG-MOSFET and $D_2$-FET with respectively $HfTe_2$ TC (**a**) and SC (**b**), for both $N_{SD} = 1.8\times10^{13}\,cm^{-2}$ and $N_{SD} = 6\times10^{11}\,cm^{-2}$. $\Delta L$ was set based on the findings for the single contacts, i.e., $\Delta L = 2.5$ nm for TC and $\Delta L = 0$ nm for SC. Device dimensions for the $D_2$-FET were taken identical to their DG-MOSFET counterparts discussed above. For the SC configuration, however, $L_{ext}$ was reduced to 4.4 m to reduce the length of the doping gate.

$V_{GS} - V_D = 0.85$ V. For a moderate bias of $V_{GS} - V_D = 0.6$ V, we obtain a carrier concentration of ~$2.4\times10^{13}\,cm^{-2}$ and a contact resistance of 42 Ωμm. Despite normalization by the gate perimeter (i.e., the current shown in Fig. 7d is the current per gate), the $E_2D_2$-FET outperforms the $D_2$-FET, demonstrating a higher value for $I_{ON}$.

## 2D–3D top-contact configuration

For the 2D–3D TC configuration, we limit ourselves to $WS_2$ for the TMD and Pt, Ru, Mo, Bi, Sb for the metal. The low melting temperature of Bi (~209 °C)[14] makes it unsuitable for direct use in fabrication. Therefore, Bi doped with Y and La (YBi and LaBi) are also considered here as alternatives, as their melting temperature is significantly increased (2020 °C and 1615 °C, respectively)[14,15]. For 2D–3D systems, transport simulations are characterized by a large computational cost. Combined with the large number of combinations of metal and surface orientation, this makes an initial screening before performing transport simulations indispensable. We consider four parameters for screening: the vdW gap and the binding energy ($E_B$), giving an indication of the interaction strength, and the n-type and p-type $SB_H$ ($nSB_H$ and $pSB_H$). A more thorough discussion is presented in the methods section. The results are shown in Fig. 8. The numerical values, as well as those for several other parameters extracted from the DFT simulations, can be found in Supplementary Table 3.

Figure 8 shows a clear correlation between the vdW gap and the binding energy, indicating that the vdW gap can indeed also be used as a measure for the interaction strength. A bimodal

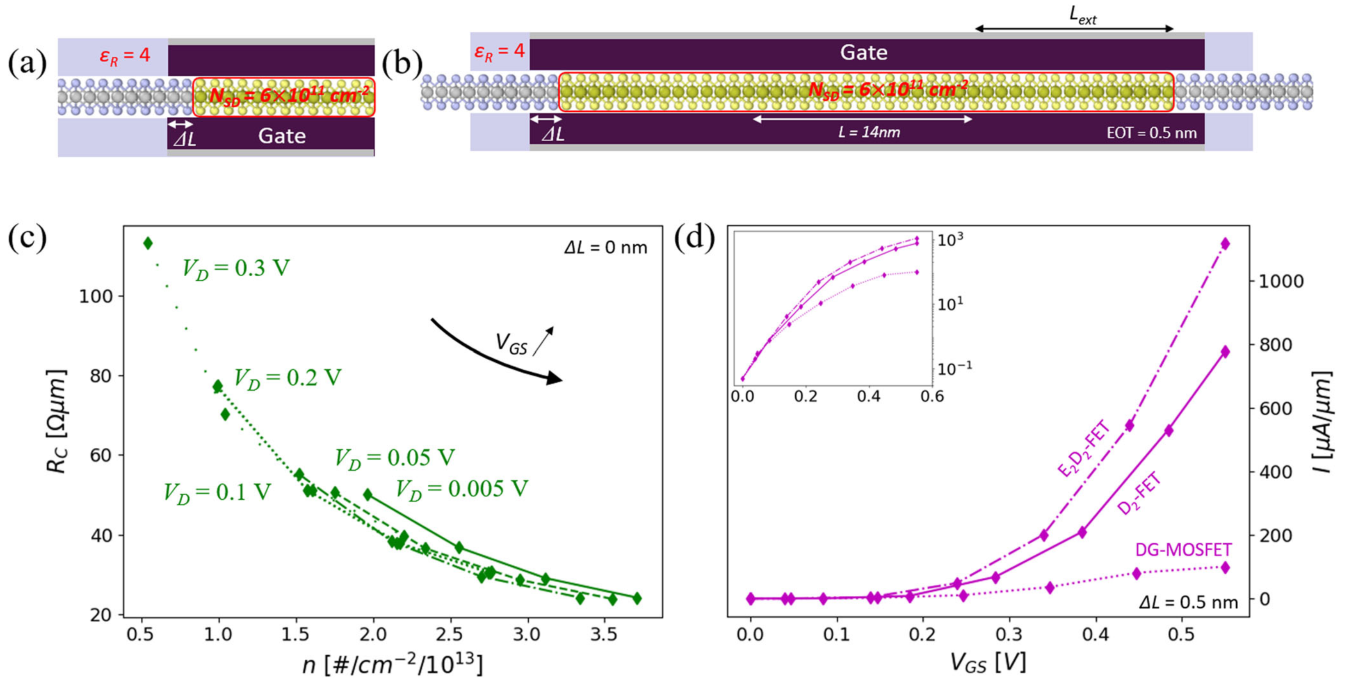


**Fig. 7 Results of dynamic doping simulations with two doping gates.** **a** Geometry of a single SC with 2 doping gates. **b** Geometry of the $E_2D_2$-FET. **c** Contact resistance and carrier concentrations of the device in **a** as a function of the gate potential for several values of the bias, $\Delta L = 0$ nm and $N_{SD} = 6\times10^{11}$ cm$^{-2}$. **d** IV curves of the device in **b** for $\Delta L = 0$ nm and $N_{SD} = 6\times10^{11}$ cm$^{-2}$ as well as the corresponding DG-MOSFET and $D_2$-FET for comparison.

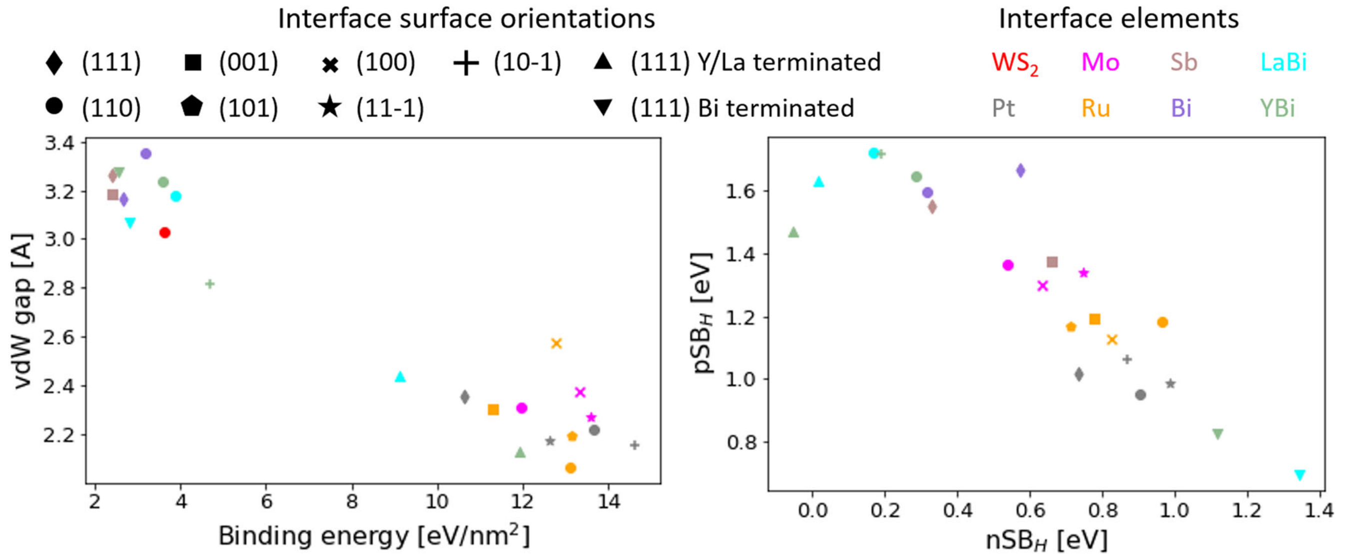


**Fig. 8 Results of DFT-based initial screening.** The $E_B$, the vdW gap, $nSB_H$, and $pSB_H$ are shown for a $WS_2$-metal TC interface for several metal and surface orientation combinations. The red dot corresponds to a $WS_2$ bilayer and acts as a reference. For YBi and LaBi, the (111) plane has two possible terminations: a layer of only Y/La atoms or a layer of Bi atoms, which are both simulated and presented separately.

model is distinguished, corresponding to interfaces that are strongly interacting: Pt, Ru, Mo and YBi and LaBi with Y/La termination, and interfaces that show less interaction than a $WS_2$ bilayer: Bi, Sb and most other YBi or LaBi surface orientations. Only one exception, YBi (10–1), with an intermediate interaction strength greater than the $WS_2$ bilayer, is found. Additionally, it can be seen that, except for a few metal-surface combinations, the estimated Schottky barrier is always several 100 meVs. From the discussion on 2D–2D interfaces, it is known that the combination of the vdW gap in a bilayer and a Schottky barrier of several 100 meVs greatly reduces device performance. Even an ohmic vdW contact introduces a contact resistance that requires a relatively high doping concentration to be mitigated. To limit the additional contact resistance of this vdW gap, the interfaces exhibiting an interaction strength greater than the bilayer may be of interest. However, these strongly interacting interfaces tend to be strongly pinned, resulting in large $SB_H$ both for n-type and p-type. Three exceptions were found with adequate values for $nSB_H$ and strong to intermediate interaction strength: YBi (10–1) and LaBi and YBi (111) terminated on Y/La. Of these three interfaces, YBi (111) is predicted to be ohmic with a negative $nSB_H$. However, YBi (111) shows a strongly corrugated structure,

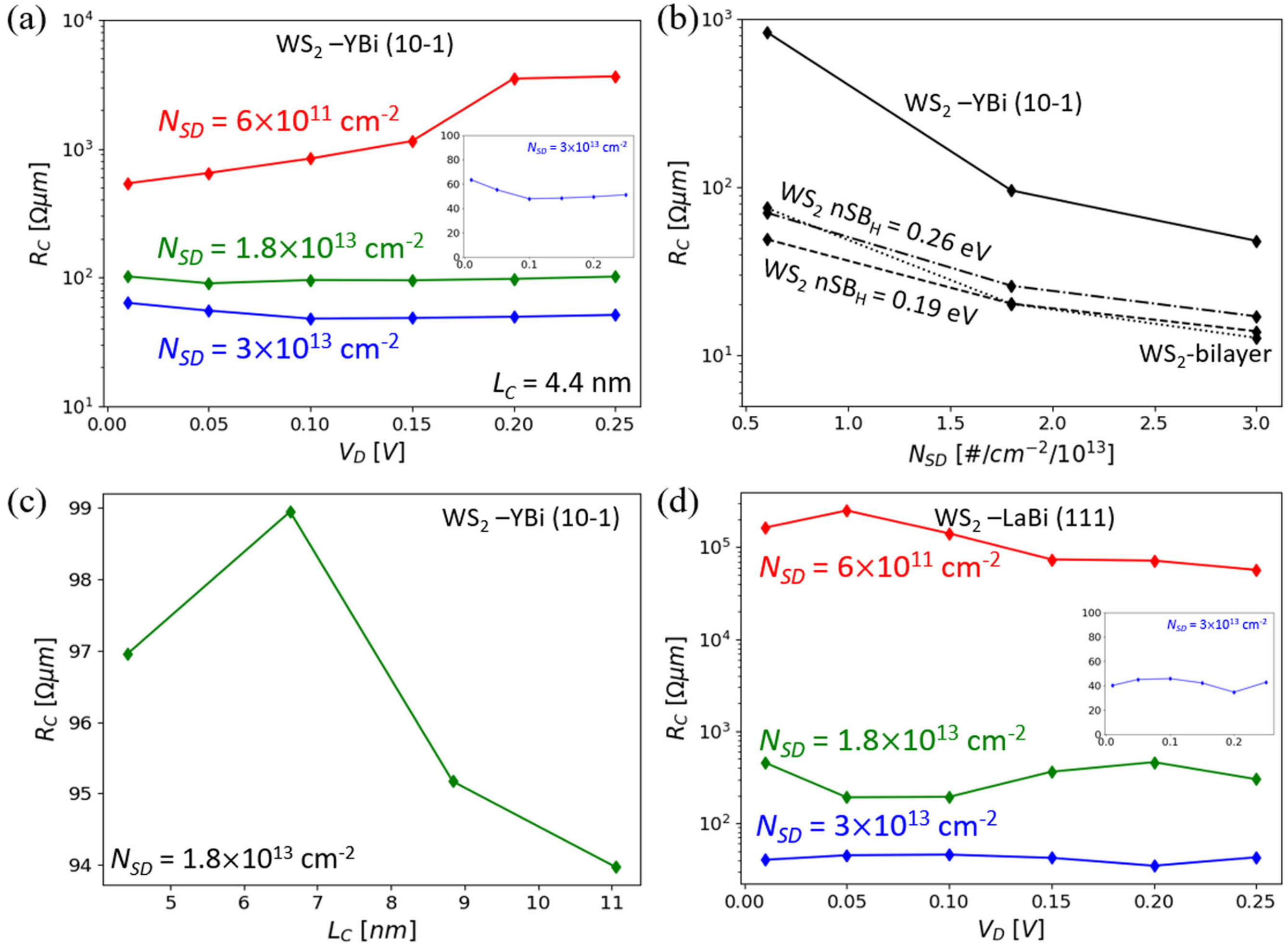


**Fig. 9 Results for the WS2 2D–3D TC.** The contact resistances extracted from a single $WS_2$-YBi (10–1) TC simulation and a single $WS_2$-LaBi (111) TC simulation are shown for several values of $L_C$ and $N_{SD}$. In **a**, $L_C$ was set to 4.4 nm and the contact resistances for the YBi (10–1) TC are shown as a function of the bias for several values of $N_{SD}$. In **b**, average $R_C$ values of a monolayer of $WS_2$ with Schottky contacts (simulated using a phenomenological self-energy term as boundary conditions)[30,31] and a bilayer of $WS_2$ vdW TC configuration are shown as a function of doping, as a reference. In **c**, $N_{SD}$ was set to $1.8{\times}10^{13}\,cm^{-2}$ and $L_C$ was varied for the YBi (10–1) TC. The graph shows the average $R_C$ over all bias conditions as a function of $L_C$. **d** shows the contact resistances for the LaBi (111) TC as a function of the bias for several values of $N_{SD}$.

destroying the 2D nature of $WS_2$, as shown in Supplementary Fig. 7. One of the consequences is a severe reduction of the band gap to 1.4 eV and a very strong sensitivity of the $SB_H$ to the local strain level and microstructure, which is not desirable in practice, especially for edge-dominated injection, as also discussed just below. We therefore restricted the transport simulations to YBi (10–1) and LaBi (111) with respectively $nSB_H = 190$ meV and $nSB_H = 15$ meV. The DOS obtained from the transport simulations provides a second way to extract an estimate for the Schottky barrier height, resulting in respectively $nSB_H = 260$ meV and $nSB_H = 540$ meV. The difference between the estimates extracted from the DFT screening and from the transport simulation is explained as follows. As discussed in further detail in the methods sections, the pure TMD parts of the transport simulation use matrix elements extracted from a pure TMD DFT simulation with relaxed atomic positions. This is done to remove any effect of corrugation due to the metal in the parts that do not have any metal. However, the relaxation process changes the band alignment and, hence, changes the Schottky barrier height. The second estimate extracted from the DOS of the transport simulation corresponds to the Schottky barrier between the metal and the relaxed structure that is not under it, while the first estimate extracted during DFT screening corresponds to a Schottky barrier value between the metal and the corrugated TMD below the metal. For edge dominated-injection, as encountered here, the second and higher barrier is probably the most relevant. Figure 9a–c show the contact resistance for the $WS_2$-YBi (10–1) TC as a function of doping concentration and contact overlap length. Figure 9c shows that the contact resistance is largely independent of the contact overlap length, implying edge injection. However, Fig. 9a indicates that the dependency on the doping concentration is significant. The contact resistances for $N_{SD} = 3{\times}10^{13}\,cm^{-2}$ and $N_{SD} = 1.8{\times}10^{13}\,cm^{-2}$ are, respectively, $R_C = 50$ Ωμm and $R_C = 95$ Ωμm. Doping concentrations lower than $N_{SD} = 1.8{\times}10^{13}\,cm^{-2}$ result in severe increases of the value of $R_C$ as well as its susceptibility to the bias. As references, contact resistances for a monolayer of $WS_2$ with pure Schottky-barrier contacts of respectively 190 meV and 260 meV, as well as a $WS_2$-bilayer vdW-limited but ohmic contact as a function of doping concentration are shown in Fig. 9b. Just like our previous results on 2D–2D contacts indicate, doping is important for tunneling through the vdW gap and thinning the Schottky barrier. However, both the absolute values of $R_C$ for the reference cases as well as their susceptibility to the doping concentrations are less than for the $WS_2$-YBi (10–1) TC. This is an indication that the intermediate interaction strength of the $WS_2$-YBi (10–1) TC does not fully mitigate the vdW gap, as the current is not only limited by the Schottky barrier. We infer that for the combination of a nonzero

$SB_H$ and this vdW-like gap, a doping concentration of at least $N_{SD} = 1.8\times10^{13}\,cm^{-2}$ is highly essential.

Figure 9d shows the contact resistance for the $WS_2$-LaBi (111) TC as a function of doping concentration. For a doping concentration of $N_{SD} = 3\times10^{13}\,cm^{-2}$, sufficient to thin the Schottky barrier, the contact resistance is found to be 40 Ωμm, i.e., slightly lower than the YBi TC. This can be attributed to the stronger interaction strength for the LaBi TC. However, for lower doping concentrations, the contact resistance increases significantly, up to several 100 kΩμm for a doping concentration of $N_{SD} = 6\times10^{12}\,cm^{-2}$. This is an indication that, despite the low Schottky barrier estimate between metal and the corrugated TMD underneath the metal, there is a significant Schottky barrier impeding the current when insufficient doping is provided. This Schottky barrier is present for edge injection between the metal and the relaxed free-standing TMD. A more in-depth discussion of the different types of TMD in the 2D–3D TC simulation is provided in the methods section.

## DISCUSSION

In this study, we show that low contact resistances can be achieved for transistors based on 2D materials. More specifically, we find that the 2D metal $HfTe_2$ can provide low n-type contact resistances for $HfS_2$ devices, both in a top contact and a side contact configuration. For $WS_2$ we find that $NbS_2$ TC can achieve moderately low p-type contact resistances although the cold metal behavior of $NbS_2$ can degrade device performance depending on the source-drain bias that is applied. For n-type $WS_2$, YBi top contacts with the surface corresponding to the (10–1) plane and LaBi top contacts with the surface corresponding to a La-rich (111) plane are predicted to have low contact resistances. In all cases, a high doping concentration is indispensable to either thin the Schottky barrier or to allow for tunneling through the vdW gap in between the metal and the 2D semiconductor. A minimally required doping concentration of $1.8\times10^{13}\,cm^{-2}$ is found to achieve contact resistances below 100 Ωμm. Increasing the doping concentration beyond this value further reduces the contact resistance, but only slightly. Going towards lower doping concentrations, on the other hand, causes a rapid and sharp increase of the contact resistance. Exceptions are $NbS_2$ TC which achieves a contact resistance of 150 Ωμm for a doping concentration of $1.8\times10^{13}\,cm^{-2}$, due to a lack of k-matching, and LaBi which requires a doping concentration of $3\times10^{13}\,cm^{-2}$ to thin its significant Schottky barrier. Finally, simulations based on $HfS_2$ with $HfTe_2$ contacts show that, by the addition of a doping gate, electrostatic doping can achieve a carrier concentration of $1.8\times10^{13}\,cm^{-2}$, allowing for the required carrier concentration for a low contact resistance. Additionally, the doping gate appears to further introduce additional contact resistance lowering effects, most likely a field-enhanced tunneling effect, beyond supplying the required carrier concentration. This phenomenon is most pronounced for top contacts as expected by the vdW tunneling mechanism. For a transistor with side contacts, the addition of a second doping gate is possible, increasing the carrier concentration further to values of $3.6\times10^{13}\,cm^{-2}$ and reaching contact resistances as low as 25 Ωμm.

## METHODS

### General outline

The methodology in this study generally consists of two parts. In a first part, Hamiltonian and/or overlap matrix elements are calculated for a metal-semiconductor interface using DFT. Secondly, these matrix elements are used in our quantum-transport solver, ATOMOS, for the calculation of transport properties and the study of device performance.

### DFT-Hamiltonian computation

Three different DFT packages were used for the geometry relaxation as well as the Hamiltonian extraction, depending on the type of interface. For $HfS_2$ (1T) – $HfTe_2$ (1T) and $WS_2$ (2H) – $NbS_2$ (2H) TC, the top metal layer and bottom semiconducting layer have the same phase as their most stable phase and the TC interface could be achieved with a DFT supercell with small dimensions. For these interfaces, we used QUANTUM ESSPRESSO[16] with the optB86b exchange-correlation functional[17], ultrasoft pseudopotentials and the Grimme DFT-D3 van der Waals correction[18]. Convergence of the total energy was used for setting the plane-wave cut-off. The convergence criteria were set to $10^{-3}$ eV for the total-energy variation between two subsequent iterations and $10^{-3}$ eV/Å for the forces acting on each ion during geometry relaxation. First a variable cell geometry relaxation was performed on the pure TMD and the metal to extract the lattice constant. Subsequently, both materials were joined in a supercell, straining both equally to achieve commensurate lattices[11] (2.4% and 3.9% for, respectively, $WS_2$-$NbS_2$ and $HfS_2$-$HfTe_2$), after which an additional fixed lattice geometry relaxation was performed to relax the atomic positions. Finally, the Bloch wavefunctions were transformed into maximally-localized Wannier functions, typically centered on the ions, using the wannier90 package[19] to extract Hamiltonian matrix elements expressed in a localized orbital basis set as required for transport[8,12].

For 2D–2D SC interfaces and the 2D–2D TC interfaces with differing phase in the top layer and bottom layer, i.e., $WS_2$ (2H) – $WTe_2$ (1T′) and $WS_2$ (2H) – $MoTe_2$ (1T′), a larger DFT cell is required. For these systems, we used OpenMX[20] with the GGA-PBE exchange-correlation functional, the pseudopotentials provided in ref. [21], the standard basis sets provided in ref. [22], and an energy cutoff of 4081 eV. The convergence criteria were set to $2.7\times10^{-5}$ eV for the self-consistent field (SCF) step and $5\times10^{-3}$ eV/Å for the forces acting on each ion during geometry relaxation and $2.7\times10^{-7}$ eV for the SCF step during Hamiltonian extraction. The same lattice constants were taken as in the TC configuration for the pure TMD to limit the influence of the DFT package. Subsequently, a heterojunction was built, again straining both subsystems equally to achieve commensurate lattices. The same values for the strain were obtained as for the 2D–2D TC. However, for the SC the materials were only strained along the orthogonal direction. Along the transport direction, the supercell dimension was relaxed together with the atomic positions in a subsequent relaxation step. The supercell dimension along the transport direction in the SC configuration were set at respectively 132 nm and 114 nm for $HfS_2$-$HfTe_2$ and $WS_2$-$NbS_2$, i.e., long enough to assume the middle of each TMD part is far enough from the interface to behave bulklike. This is required to obtain matrix elements which can represent bulklike TMD behavior. No further Wannierization process is required as the provided matrix elements are already expressed in a localized orbital basis set.

For 2D–3D TC interfaces, we used CP2K[23] with the GTH-PBE exchange-correlation functional[24], the DZVP-MOLOPT-SR-GTH basis sets from ref. [25] and the Grimme DFT-D3 van der Waals correction. The energy cutoff was set based on convergence tests on the atomic species in the DFT cell. The convergence criteria were set to $10^{-6}$ eV for the SCF step and $5.2\times10^{-2}$ eV/Å for the forces acting on each ion during geometry relaxation. The building of TC supercells was performed in a similar fashion as the 2D–2D interfaces, except that here, multiple supercells are possible depending on the surface orientation of the 3D metal at the interface and the thickness of the metal film. The thickness of the metal film was set to 10 Å. Surface orientations were selected based on the existence of a supercell with both a limited strain and cell dimensions small enough to achieve realistic simulation times. The upper limit for the strain was set at 1.5% strain in both TMD and metal.

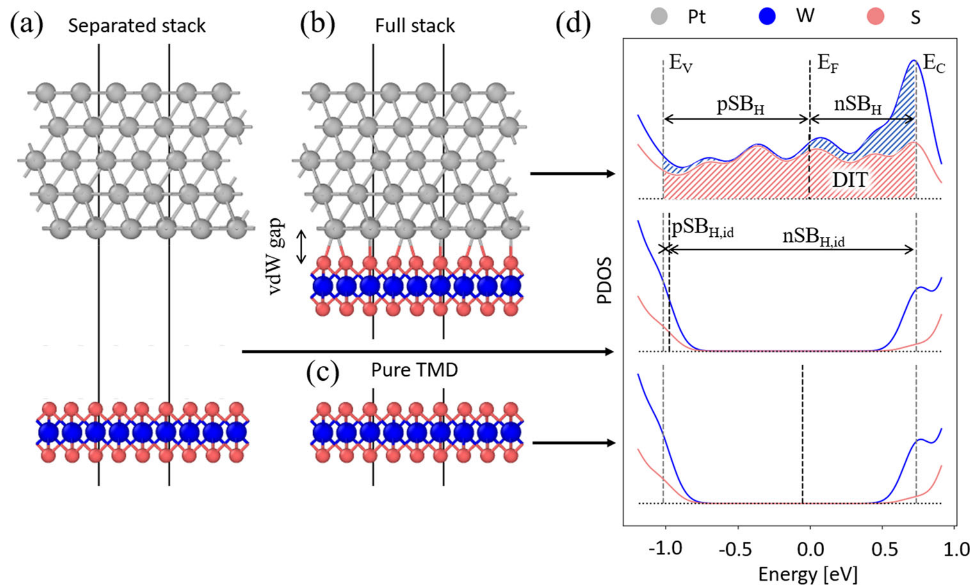


**Fig. 10 Illustration of the methodology used to extract parameters for a 2D–3D TC. a–c** show, respectively, the atomic structure of the top contact with a vacuum inserted in between the TMD and the metal, the original TC and the pure TMD. **d** shows the PDOS of the TMD atoms in the different structures and how parameters are extracted from the PDOS. The black lines in the atomic structures denote the simulation cell boundaries. For the pure TMD and separate stack, tails can be seen in the PDOS that extend from the conduction band and the valence band into the band gap as result of Gaussian broadening in plotting the DOS. They do not correspond to physical states and are not included in the DIT.

In all cases, spin–orbit coupling was neglected, a vacuum layer of 20 Å was introduced along the out-of-plane direction to prevent spurious interaction of periodic images and convergence of the total energy was used to determine the density of the Monkhorst–Pack *k*-point grid for the Brillouin-zone integration.

It is a well-known fact that DFT can give wrong estimates of the band gap and can make errors in the band alignment. Concerning the band gap, we have performed checks that the band gaps obtained with our Hamiltonian elements, at least for the pure semiconducting TMD, are close to experimental values. Concerning the band alignment, a major contribution to wrong band alignments is the arbitrariness of the vacuum energy by the use of pseudopotentials. This contribution is especially of importance when comparing different DFT simulations. This effect has been compensated for as explained in the section on DFT-based screening. Other contributions to errors in the band alignment that are more difficult to compensate for will indeed introduce errors in the numerical values of our results. Observed trends in DFT, simulations, are, however, often found to be correct.

Finally, we have been performing additional checks, including the use of hybrid functionals which is known to reduce the problems of DFT for several semiconductors and insulators, to check within the best of our knowledge that the results were sound, consistent and as free as possible from numerical artefacts. A full discussion of these tests is, however, outside the scope of this work.

## Quantum transport solver

ATOMOS enables the simulation of quantum transport in devices using the Green's function formalism[26,27] within the real- and mode-space framework[8,28]. Transport can be either ballistic or dissipative, including electron-phonon scattering within the self-consistent Born approximation[29]. In this work, a real-space description was employed and scattering was included in all the simulations. The Hamiltonian and overlap matrix elements are obtained from DFT as described in the procedure above. For the electron-phonon interaction, we used the DFT-computed parameters provided in ref. [4]. The systems in this work are characterized by periodicity in the transversal direction, captured by 10 k-points along ½ the Brillouin zone (the other half is obtained by symmetry) for the 2D–2D systems, and 5 k-points for the relatively larger 2D–3D systems.

## DFT-based screening

Figure 10 shows the methodology on how several parameters of interest can be extracted from the atomic structure and its corresponding DOS. The binding energy, a measure for the interaction strength, is computed as the difference between the total energy of a DFT simulation of the full stack and the total energies of DFT simulations of the TMD and metallic parts of the stack.

$$E_B = E_{tot}(\text{TMD}) + E_{tot}(\text{metal}) - E_{tot}(\text{full stack}) \quad (1)$$

A second estimate for the interaction strength can be found from the size of the vdW gap, which is expected to be lower for stronger interactions. An estimate for the $SB_H$ is obtained from the DOS of the DFT simulation. The bottom of the conduction band ($E_C$) and top of the valence band ($E_V$) are obtained from a DOS calculation of a separate DFT simulation containing only the TMD part of the stack. The difference between the bottom of the conduction band (top of the valence band) and the Fermi level of the full stack gives an estimate of the $nSB_H$ ($pSB_H$). In addition, to obtain the ideal Schottky barrier height in the Schottky–Mott limit ($SB_{H,id}$), we further performed a DFT simulation of the stack with vacuum inserted in between the TMD and the metal (see Fig. 10). This vacuum prevents direct interaction between the two surfaces and therefore prevents Fermi-level pinning. The difference between $SB_H$ and $SB_{H,id}$, $\Delta_F$, provides an estimate of the Fermi-level pinning. As energy levels of different simulations are compared, we first shifted all DOS energies to align the lowest energy deep-valence state of the TMD. As these deep-valence states corresponds to core electrons of certain atoms, they are affected only slightly by their surroundings and should provide a good reference to eliminate the arbitrary shift in energies

introduced by the DFT simulation.

$$\begin{aligned} nSB_H &= E_C(\text{TMD}) - E_F(\text{full stack})\; nSB_{H,id} = E_C(\text{TMD}) - E_F(\text{separated stack}) \\ pSB_H &= E_F(\text{full stack}) - E_V(\text{TMD})\; pSB_{H,id} = E_F(\text{separated stack}) - E_V(\text{TMD}) \\ \Delta_F &= E_F(\text{separated stack}) - E_F(\text{full stack}) \end{aligned} \quad (2)$$

A third parameter of interest when comparing contacts is the density of interface traps induced by the metal. A DIT estimate can be obtained from the DOS calculation, by integrating the projected DOS (PDOS) of the TMD atoms of the full stack within the bandgap.

$$\text{DIT} = \int_{E_V}^{E_C} \text{PDOS}(E)\text{d}E \quad (3)$$

Only 2D–3D interfaces which show interesting values for the Schottky barrier height and interaction strength were simulated using the transport solver. For these interfaces, matrix elements were extracted. As in OpenMX, these elements are expressed in a localized orbital basis set and no Wannierization step is required. Due to interactions between metal and TMD in the stack, the atomic structure of the TMD part can be slightly corrugated and the electronic states do not always correspond well with bulk TMD, as was the case for 2D–2D TC. Therefore, the matrix elements for bulk TMD were extracted from a separate DFT simulation containing only the TMD part of the stack. The TMD part was relaxed before extraction, keeping the lattice dimensions fixed to preserve a commensurate system. On-site energies corresponding to the lowest energy deep-valence state were shifted to eliminate arbitrary shifts introduced by the DFT simulations.

## DATA AVAILABILITY

The data that support the findings of this study are available from the corresponding author upon reasonable request.

## CODE AVAILABILITY

Access to the code that is used in this study is restricted by imec legal policy.

Received: 28 October 2022; Accepted: 18 May 2023;
Published online: 31 May 2023

## REFERENCES

1. Novoselov, K. S. et al. Two-dimensional atomic crystals. *Proc. Natl Acad. Sci. USA* **102**, 10451–10453 (2005).
2. Novoselov, K. S., Mishchenko, A., Carvalho, A. & Castro Neto, A. H. 2D materials and van der Waals heterostructures. *Science* **353**, 9439 (2016).
3. Radisavljevic, B., Radenovic, A., Brivio, J., Giacometti, V. & Kis, A. Single-layer $MoS_2$ transistors. *Nat. Nanotechnol.* **6**, 147–150 (2011).
4. Huang, Z., Zhang, W. & Zhang, W. Computational search for two-dimensional $MX_2$ semiconductors with possible high electron mobility at room temperature. *Materials* **9**, 716 (2016).
5. Schwierz, F., Pezoldt, J. & Granzner, R. Two-dimensional materials and their prospects in transistor electronics. *Nanoscale* **7**, 8261–8283 (2015).
6. Zhao, Y. et al. Doping, contact and interface engineering of two-dimensional layered transition metal dichalcogenides transistors. *Adv. Funct. Mater.* **27**, 1603484 (2017).
7. Afzalian, A. & Pourtois, G. ATOMOS: an atomistic modelling solver for dissipative DFT transport in ultra-scaled $HfS_2$ and black phosphorus MOSFETs. In *2019 International Conference on Simulation of Semiconductor Processes and Devices (SISPAD)* 1–4 (SISPAD, 2019).
8. Afzalian, A. Ab initio perspective of ultra-scaled CMOS from 2D-material fundamentals to dynamically doped transistors. *Npj 2D Mater. Appl.* **5**, 1–13 (2021).
9. Nath, A. et al. In search of quantum-limited contact resistance: understanding the intrinsic and extrinsic effects on the graphene–metal interface. *2D Mater.* **3**, 025013 (2016).
10. Allain, A., Kang, J., Banerjee, K. & Kis, A. Electrical contacts to two-dimensional semiconductors. *Nat. Mater.* **14**, 1195–1205 (2015).
11. Duflou, R., Houssa, M. & Afzalian, A., Electron-phonon scattering in cold-metal contacted two-dimensional semiconductor devices. In *International Conference on Simulation of Semiconductor Processes and Devices (SISPAD)* 94–97 (SISPAD, 2021).
12. Afzalian, A., Akhoundi, E., Gaddemane, G., Duflou, R. & Houssa, M. Advanced DFT–NEGF transport techniques for novel 2-D material and device exploration including $HfS_2/WSe_2$ van der Waals heterojunction TFET and $WTe_2/WS_2$ metal/semiconductor contact. *IEEE Trans. Electron. Devices* **68**, 5372–5379 (2021).
13. Afzalian, A., Zubair, A. & Julien, R. Forked contact and dynamically-doped nanosheets to enhance Si and 2D materials device at the limit of scaling. *Solid State Electron.* **199**, 108524 (2023).
14. Schmidt, F. A., McMasters, O. D. & Lichtenberg, R. R. The yttrium-bismuth alloy system. *J. Less Common Met.* **18**, 215–220 (1969).
15. Nomura, K., Hayakawa, H. & Ono, S. The lanthanum-bismuth alloy system. *J. Less Common Met.* **52**, 259–269 (1977).
16. Giannozzi, P. et al. QUANTUM ESPRESSO: a modular and open-source software project for quantum simulations of materials. *J. Phys. Condens. Matter* **21**, 155–178 (2009).
17. Klimeš, J., Bowler, D. R. & Michaelides, A. Chemical accuracy for the van der Waals density functional. *J. Phys. Cond. Matter* **22**, 022201 (2010).
18. Grimme, S., Antony, J., Ehrlich, S. & Krieg, H. A consistent and accurate ab initio parametrization of density functional dispersion correction (DFT-D) for the 94 elements H-Pu. *J. Chem. Phys.* **132**, 154104 (2010).
19. Mostofi, A. A. et al. An updated version of wannier90: a tool for obtaining maximally-localised Wannier functions. *Comput. Phys. Commun.* **185**, 2309 (2014).
20. Neale, M. et al. OpenMx 2.0: extended structural equation and statistical modeling. *Psychometrika* **81**, 535–549 (2016).
21. Ozaki, T. Variationally optimized atomic orbitals for large-scale electronic structures. *Phys. Rev. B* **67**, 155108 (2003).
22. Ozaki, T. & Kino, H. Numerical atomic basis orbitals from H to Kr. *Phy. Rev. B* **69**, 195113 (2004).
23. Kühne, T. D. et al. CP2K: an electronic structure and molecular dynamics software package – Quickstep: efficient and accurate electronic structure calculations. *J. Chem. Phys.* **152**, 194103 (2020).
24. Krack, M. Pseudopotentials for H to Kr optimized for gradient-corrected exchange-correlation functionals. *Theor. Chem. Acc.* **114**, 145–152 (2005).
25. VandeVondele, J. & Hutter, J. Gaussian basis sets for accurate calculations on molecular systems in gas and condensed phases. *J. Chem. Phys.* **127**, 114105 (2007).
26. Keldysh, P. Diagram technique for nonequilibrium processes. *Sov. Phys. JETP* **20**, 1018 (1965).
27. Kadanoff, P. & Baym, G. *Quantum Statistical Mechanics* (Benjamin, 1962).
28. Afzalian, A. et al. Physics and performance of III-V nanowire broken-gap heterojunction TFETs using an efficient tight-binding mode-space NEGF model enabling million-atom nanowire simulations. *J. Phys. Condens. Matter* **30**, 254002 (2018).
29. Afzalian, A. Computationally efficient self-consistent Born approximation treatments of phonon scattering for coupled-mode space non-equilibrium Green's functions. *J. Appl. Phys.* **110**, 094517 (2011).
30. Afzalian, A. & Flandre, D. Computational study of dopant segregated nanoscale Schottky barrier MOSFETs for steep slope, low SD-resistance and high on-current gate modulated resonant tunneling FETs. *Solid State Electron.* **65-66**, 123–129 (2011).
31. Afzalian, A. & Flandre, D. Discrete random dopant fluctuation impact on nanoscale dopant-segregated Schottky-barrier nanowires. *IEEE Electron. Device Lett.* **33**, 1228–1230 (2012).

## ACKNOWLEDGEMENTS

This research was funded by the FWO as part of the PhD fellowship 1100321N. A.A. thanks Dr. Gouri Sankar Kar and Dr. Cesar Javier Lockhart de la Rosa for management support. R.D. acknowledges the support of Michiel van Setten, Sergiu Clima, Christopher Pashartis, Kiroubanand Sankaran, Albert de Jamblinne de Meux, and Benoit Van Troeye related to advice on the DFT simulations and the use of their simulation scheduler toolkit.

## AUTHOR CONTRIBUTIONS

A.A. developed the theory, simulation code, and concepts (e.g., the $D_2$-FET). R.D. and A.A. performed the 2D–2D metal-semiconductor first-principle simulations. R.D. and G.P. developed the algorithms used to build the 3D–2D interface models, performed the first-principle simulations, and analyzed the resulting data. R.D. and A.A.

performed the transport simulations and the related algorithm optimizations, analyzed the data and wrote the manuscript. M.H., G.P., and A.A. supervised the work. All authors discussed the results and proofread the manuscript.

## COMPETING INTERESTS

The authors declare no competing interests.

## ADDITIONAL INFORMATION

**Supplementary information** The online version contains supplementary material available at https://doi.org/10.1038/s41699-023-00402-3.

**Correspondence** and requests for materials should be addressed to Aryan Afzalian.

**Reprints and permission information** is available at http://www.nature.com/reprints

**Publisher's note** Springer Nature remains neutral with regard to jurisdictional claims in published maps and institutional affiliations.

**Open Access** This article is licensed under a Creative Commons Attribution 4.0 International License, which permits use, sharing, adaptation, distribution and reproduction in any medium or format, as long as you give appropriate credit to the original author(s) and the source, provide a link to the Creative Commons license, and indicate if changes were made. The images or other third party material in this article are included in the article's Creative Commons license, unless indicated otherwise in a credit line to the material. If material is not included in the article's Creative Commons license and your intended use is not permitted by statutory regulation or exceeds the permitted use, you will need to obtain permission directly from the copyright holder. To view a copy of this license, visit http://creativecommons.org/licenses/by/4.0/.

© The Author(s) 2023